RSC Advances

PAPER

Check for updates

Fabrication of TiO$_2$ on porous g-C$_3$N$_4$ by ALD for improved solar-driven hydrogen evolution†

Wei-Szu Liu, [ID] Li-Chen Wang, Tzu-Kang Chin, Yin-Cheng Yen and Tsong-Pyng Perng [ID] *

Porous graphitic carbon nitride (P-g-C$_3$N$_4$) thin sheets were fabricated by a one-step calcination of a mixture of urea, melamine, and ammonia chloride at 550 °C. P-g-C$_3$N$_4$ showed 48% higher photocatalytic H$_2$ production from methanol aqueous solution than conventional urea-derived graphitic carbon nitride (g-C$_3$N$_4$) because the existence of numerous pores reduces the recombination rate of charge carriers. In order to further enhance the photocatalytic activity, TiO$_2$ was uniformly deposited on P-g-C$_3$N$_4$ by 60–300 cycles of atomic layer deposition (ALD) to form the TiO$_2$@P-g-C$_3$N$_4$ composite. They exhibited much higher photocatalytic hydrogen production rates than both TiO$_2$ and P-g-C$_3$N$_4$. Among all composites, the sample deposited with 180 ALD cycles of TiO$_2$ showed the highest H$_2$ production because of optimal diffusion length for electrons and holes. It also performed better than the sample of g-C$_3$N$_4$ deposited with 180 cycles of TiO$_2$.

1. Introduction

Graphitic carbon nitride, a thermally and chemically stable, cheap, and abundant semiconductor material, is a visible light-driven photocatalyst. It is considered as a promising material for producing hydrogen from water splitting. Wang *et al.*[1] first discovered that this metal-free photocatalyst could be easily obtained by pyrolysis of cyanamide and it could generate H$_2$ from water under visible light illumination. However, the water splitting efficiency is usually limited by fast recombination of charge pairs.[2,3] Furthermore, it is difficult to generate a large amount of H$_2$ under visible light illumination by one-step photoexcitation because a good photocatalyst needs to fulfill three requirements: suitable band-edge positions, appropriate band gap, and long-term durability.[4,5] In order to improve the water splitting efficiency, a heterostructure composed of a pair of photocatalysts may fulfill the requirements and also decrease the recombination rate of charge carriers.[6,7]

There are several oxide candidates to couple with g-C$_3$N$_4$ to enhance the photocatalytic H$_2$ production, such as WO$_3$,[8,9] TiO$_2$,[10–12] *etc.* There have been some reports on the TiO$_2$/g-C$_3$N$_4$ system.[10–17] However, most of the studies employed TiO$_2$ as a support to deposit g-C$_3$N$_4$. Previously, we have successfully deposited TiO$_2$ thin films on different supports for photocatalytic applications.[18–20] In this study, TiO$_2$ film was deposited on porous g-C$_3$N$_4$ by ALD with various thicknesses, and the

physical and chemical properties were investigated. The aim is to use TiO$_2$/g-C$_3$N$_4$ composite as a photocatalyst to enhance H$_2$ evolution from water under solar light irradiation.

2. Experimental

A. Sample preparation

5 g urea (Showa Chemical, 99.0%), 2.5 g melamine (Showa Chemical, 99.5%), and 5 g ammonium chloride (Showa Chemical, 99.5%) were grinded by an agate mortar and then placed in an Al$_2$O$_3$ crucible with a cover. It was heated in a muffle furnace at 550 °C for 4 h in air. A yellow solid powder, P-g-C$_3$N$_4$, was obtained after cooling to room temperature. The conventional g-C$_3$N$_4$ was also prepared by heating urea under the same condition. To prepare TiO$_2$@P-g-C$_3$N$_4$ composite, the P-g-C$_3$N$_4$ powder was first added into ethanol, ultrasonically vibrated for 30 min, and the solution was then dropped on a silicon wafer, followed by drying at 80 °C. Next, the sample was placed into the ALD chamber, and TiO$_2$ film was deposited onto the P-g-C$_3$N$_4$ with different cycle numbers. The ALD was conducted in a home-built horizontal-flow type reactor with the substrate temperature maintained at 100 °C, as described previously.[21] TiCl$_4$ and H$_2$O were used as the precursors for titanium and oxygen, respectively. Each cycle consisted of a TiCl$_4$ pulse for 0.2 s, a purge with N$_2$ for 7 s, followed by a H$_2$O pulse for 0.1 s, and a second purge with N$_2$ for 7 s to remove excess precursor and by-products. Hereafter, Ti60–CN, Ti180–CN, and Ti300–CN stand for the samples of P-g-C$_3$N$_4$ deposited with TiO$_2$ by 60, 180, and 300 cycles of ALD, respectively. The as-deposited TiO$_2$ was amorphous, so the samples were further annealed in a rapid thermal annealing (RTA) system at 450 °C

Department of Materials Science and Engineering, National Tsing Hua University, Hsinchu 30010, Taiwan. E-mail: tpperng@mx.nthu.edu.tw; Fax: +886-3-5723857; Tel: +886-3-5742634

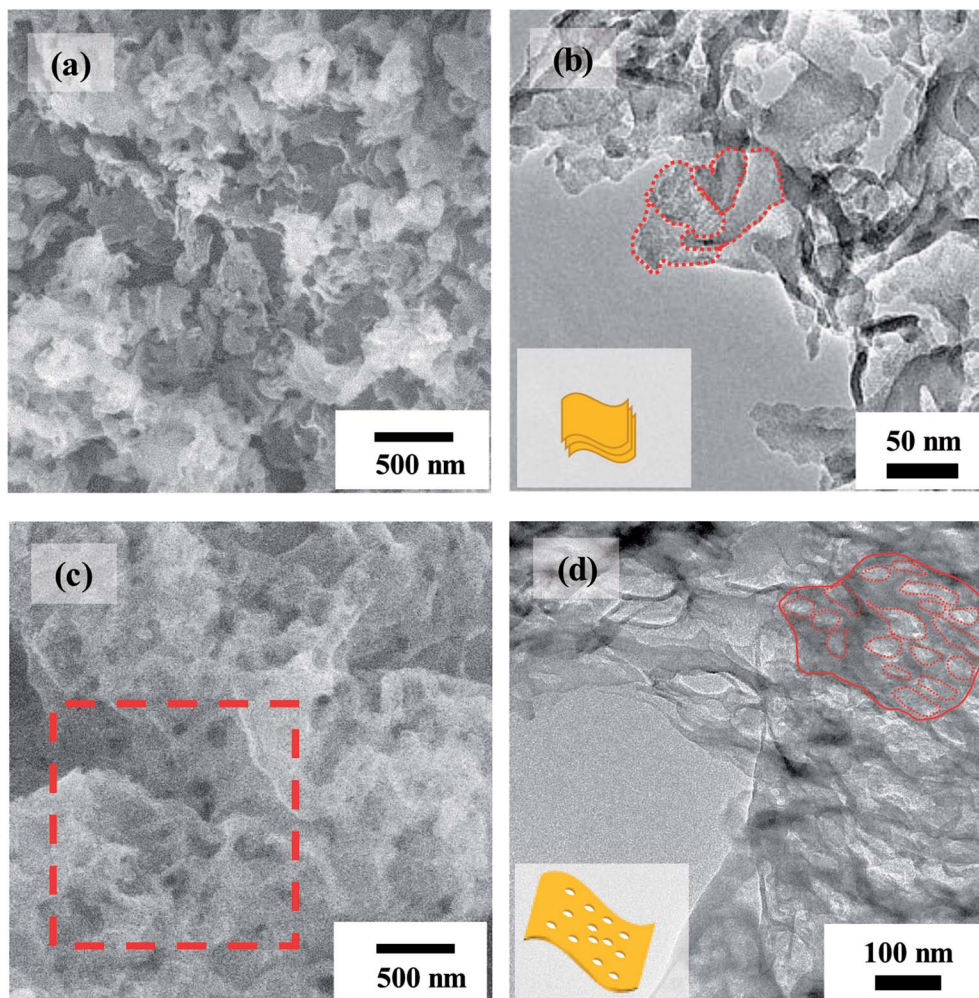† Electronic supplementary information (ESI) available. See DOI: 10.1039/c8ra05126g

Fig. 1 (a) SEM and (b) TEM images of g-C$_3$N$_4$. (c) SEM and (d) TEM images of P-g-C$_3$N$_4$. The selected region in red dashed square in (c) is enlarged and displayed in Fig. 4(a). The insets in (b) and (d) are schematic illustrations of overlapped nanosheets and porous sheet in the marked regions of g-C$_3$N$_4$ and P-g-C$_3$N$_4$, respectively.

for 2 min in Ar to obtain anatase phase. For photocatalysis test, Pt nanoparticles were further deposited on the samples by 30 cycles of ALD as a cocatalyst. Oxygen and trimethyl (methyl-cyclopentadienyl) platinum (IV) (MeCpPtM$_3$) were used as the precursors. Each cycle consisted of a MeCpPtM$_3$ pulse for 0.5 s, a purge with N$_2$ for 15 s, followed by an oxygen pulse for 2 s, and a second purge with N$_2$ for 20 s. The process of depositing Pt by ALD has also been described previously.[22]

B. Sample characterization

The crystalline structure of the samples was evaluated by X-ray diffraction (XRD, D2, Perkiment) with Cu K$_\alpha$ radiation. The surface morphologies and elementary compositions of the specimens were examined by a field emission scanning electron microscope (SEM, Hitachi SU-8010) equipped with an energy dispersive X-ray (EDX) spectrometer. High-resolution transmission electron microscopic (HRTEM) and transmission electron microscopic (TEM) examinations were conducted at 200 kV by JEM F200 (JEOL) and TEM 2010 (JEOL), respectively. The specific surface area was estimated by using the Brunauer–

Emmett–Teller (BET) method on a TriStar 3000 gas adsorption analyzer with the degassing temperature at 120 °C for 5 h. To examine the growth rate of TiO$_2$, the film was deposited by the same ALD process on silicon wafer and the thickness was detected by an ellipsometer (Sentech SER800). Fourier transform infrared spectroscopic (FTIR, Thermo iS10) analysis was conducted using KBr pallet samples. The chemical states on the surface were determined by X-ray photoelectron spectroscopy (XPS, PHI 5000 Versaprobe II, Ulvac PHI Inc.) with Al K$_\alpha$ radiation. The photoelectrons were collected into the analyzer with a pass energy of 23.5 eV and at a collection step 0.1 eV. Chemical shifts resulting from the charging effect were calibrated by fixing the C 1s peak of the surface carbonaceous contaminants at 284.8 eV. The loading of Pt was analyzed by inductively coupled plasma-mass spectrometer (ICP-MS, Agilent 7500ce). Thermogravimetric analysis (TGA) at a heating rate of 20 °C min^{-1} was carried out on a Netzsch STA 409 analyzer in Ar. The absorption edges were analyzed using UV-vis spectrometry (HITACHI 3010) in a diffused reflectance mode with a scanning range from 750 to 350 nm. Aluminum oxide (Al$_2$O$_3$), which is considered to exhibit total reflections, was used as the
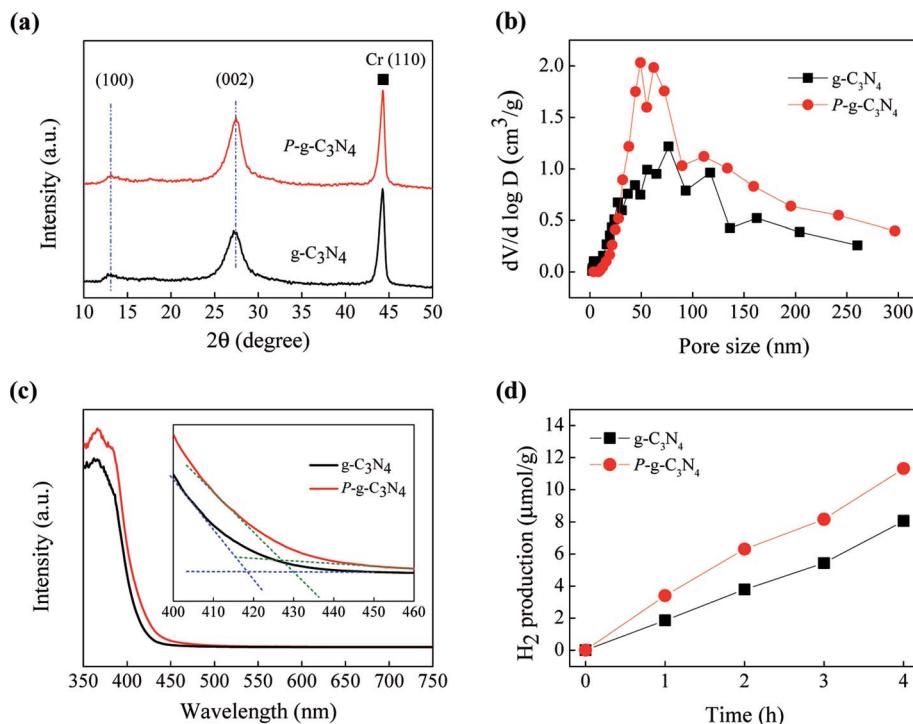
Fig. 2 Comparison between P-g-C_3N_4 and g-C_3N_4. (a) XRD patterns, (b) pore size distributions, (c) UV-vis diffuse reflectance spectra, and (d) solar-driven H_2 evolution from 20 vol% methanol aqueous solution.

reference for all of the measurements. The diffused reflectance was then converted into absorption according to the Kubelka–Munk formula. Confocal photoluminescence (PL) spectroscopy was conducted using a He–Cd laser with the wavelength of 325 nm as the excitation light source.

C. Photocatalytic hydrogen evolution

The photocatalytic H_2 evolution reaction was carried out in a quartz cell using a 300 W Xe lamp as the light source with

a solar filter. The photocatalyst sample (5 mg) was immersed into a 25 mL aqueous methanol solution (20 vol%) under magnetic stirring. The evolved H_2 gas was collected and analyzed by a gas chromatograph (GC, Shimadzu GC-2014) at 100 °C using a 5 Å molecular sieve in the column and argon as the carrier gas.

D. Photoelectrochemical measurement

The photoelectrochemical measurement was conducted by an electrochemical workstation (Autolab PGSTAT128N) using the prepared samples as the working electrode with an active area of 1.5 cm^2, Ag/AgCl electrode as the reference electrode, and Pt as the counter electrode. The electrolyte was 0.5 M Na_2SO_4 aqueous solution, and the light source was a 150 W Xe lamp with a solar filter. The preparation of working electrodes from the powder samples is as follows: first, 0.15 g powder was well dispersed into 1.5 mL 50 vol% ethanol aqueous solution. Next, it was added with 0.5 mL isobutanol (Echo Chemical), followed by 0.06 g polyethylene glycol (PEG, Alfa Aesar). The slurry was
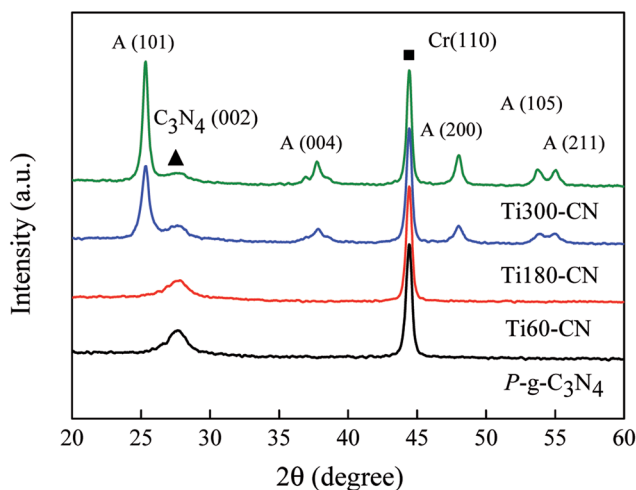

Fig. 3 XRD patterns of the samples. Cr is added as an internal standard, and the symbols of square (■) and triangle (▲) show the peak positions of Cr (110) and g-C_3N_4 (002), respectively. The other diffraction peaks are ascribed to the anatase phase.

Table 1 Crystallite size of TiO_2 (101), thickness of TiO_2, and specific surface area for fabricated samples

Sample	Crystallite size (nm) on TiO_2 (101)	Thickness of TiO_2 (nm)	Specific surface area (m^2 g^{-1})
g-C_3N_4	—	—	101.1
P-g-C_3N_4	—	—	79.0
Ti60–CN	—	4.05	55.2
Ti180–CN	9.5	12.64	41.9
Ti300–CN	16.1	24.69	27.3

then screen-printed on a fluorine-doped tin oxide (FTO) glass. After drying, the working electrode was further heated at 450 °C for 30 min. For preparation of the working electrode of TiO_2 sample, a TiO_2 thin film was deposited on FTO glass by 180 cycles of ALD, which was further annealed at 450 °C for 2 min in Ar by the RTA system.

3.   Results and discussion

A.   Comparison of g-C_3N_4 and P-g-C_3N_4 characteristics

Fig. 1 shows the comparison of g-C_3N_4 and P-g-C_3N_4 in morphology. Both SEM and TEM images indicate that g-C_3N_4 is in the form of flat film consisting of many overlapped nano-sheets, whereas P-g-C_3N_4 is formed as a large-area thin sheet full of pores. The schematic illustrations of the nanostructure of g-C_3N_4 and P-g-C_3N_4 are shown in the insets of Fig. 1(b) and (d), respectively.

The XRD patterns of g-C_3N_4 and P-g-C_3N_4 are shown in Fig. 2(a). There are two distinct diffraction peaks. The stronger XRD peak (002) at 27.4° is due to inter-planar stacking of the conjugated aromatic system, and the other weak peak (100) at 13.1° is attributed to an in-plan structural packing motif.[23–26] There is no peak shift of porous structure, as calibrated by the Cr (110) peak. However, compared to g-C_3N_4, the smaller full width at half maximum (FWHM) and higher intensity of (002) peak of P-g-C_3N_4 implies a better crystallinity and more layers of P-g-C_3N_4.[27,28] Fig. 2(b) shows the pore size distribution of the two carbon nitride samples. Because of the addition of NH_4Cl, numerous pores in the range of 40 to 80 nm were formed in P-g-C_3N_4 by gas release during the thermal treatment.[23]

Fig. 2(c) shows the optical absorption spectra of the two samples. The absorption edges are at about 418 and 427 nm, corresponding to band gaps of 2.97 and 2.90 eV, for g-C_3N_4 and P-g-C_3N_4, respectively. The larger band gap of g-C_3N_4 may be due to the quantum effect because it is in the form of thinner nanosheets, as also evidenced in the XRD pattern.[14,29,30] Fig. 2(d) shows that P-g-C_3N_4 generates 48% higher average amount of H_2 than g-C_3N_4 because of the existence of numerous pores that could shorten the diffusion length of charge carriers, which may lead to lower recombination rate.[14,31,32] Therefore, in this study P-g-C_3N_4 was used as a support to deposit TiO_2 with different ALD cycles for further experiments.

B.   Characteristics of TiO_2@P-g-C_3N_4 composites

The XRD patterns of the samples are illustrated in Fig. 3. Cr powder is used as an internal standard to calibrate the position and intensity of diffraction peaks. Except Ti60–CN, in which the crystallite size of TiO_2 might be too small to be observed by
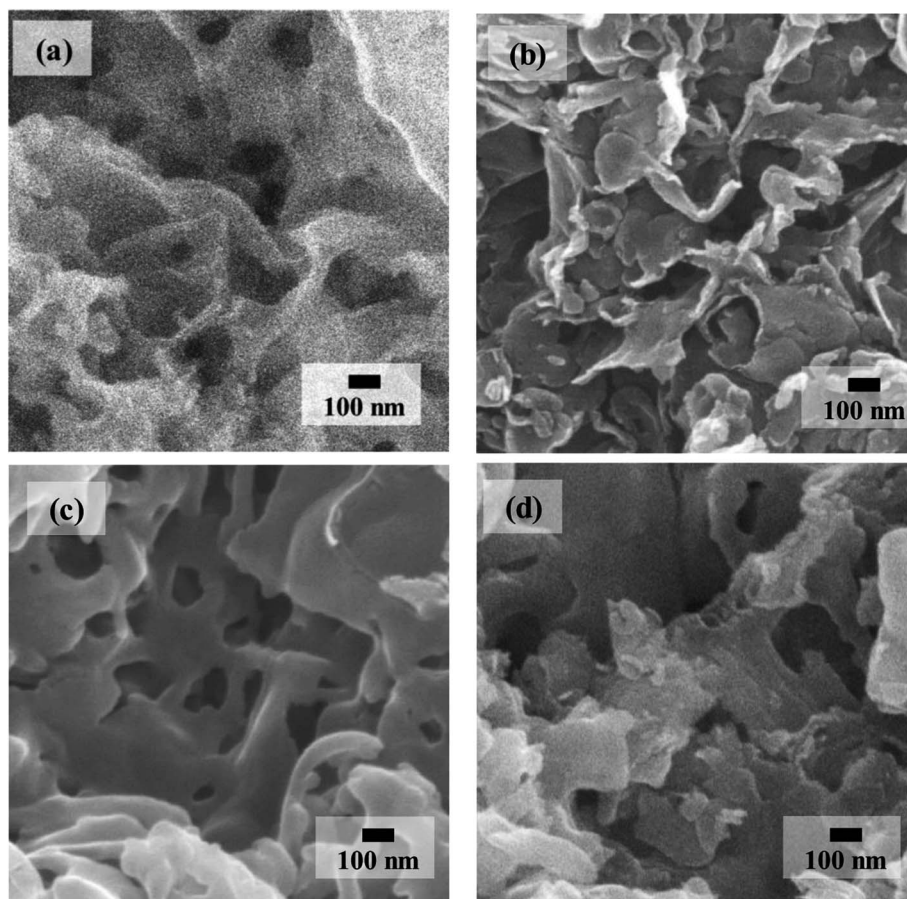

Fig. 4   SEM images of the samples. (a) As-prepared P-g-C_3N_4 enlarged from Fig. 1(c). (b) Ti60–CN, (c) Ti180–CN, and (d) Ti300–CN. All composites were treated at 450 °C for 2 min by RTA in Ar.
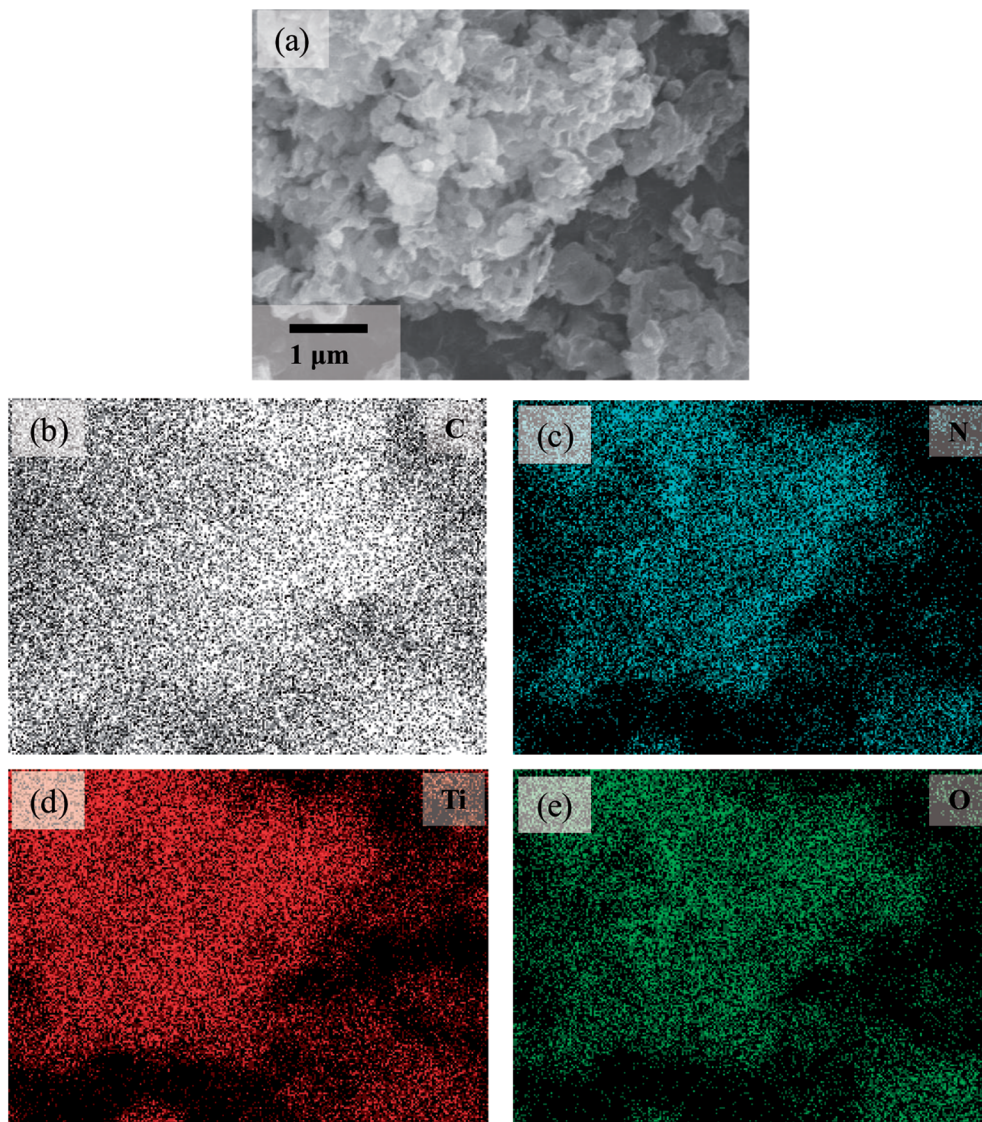
Fig. 5 EDX mapping of the Ti180–CN sample. (a) SEM micrograph and the elemental mappings of (b) C, (c) N, (d) Ti, and (e) O.

XRD, some new peaks from the anatase phase are present in the $TiO_2@P\text{-}g\text{-}C_3N_4$ composites. The crystallite sizes of TiO_2 in Ti180–CN and Ti300–CN are calculated by the Scherrer's equation and listed in Table 1. It is seen that both the peak intensity and crystallite size of the anatase phase increase with the TiO_2 cycle number. There is basically no peak shift, as calibrated by the Cr (110).

In order to further confirm molecular structures of P-g-C_3N_4, TiO_2, and $TiO_2@P\text{-}g\text{-}C_3N_4$ composites, FTIR spectra were measured, as shown in Fig. S1.† For pure P-g-C_3N_4, the absorption bands between 1200–1700 cm^{-1} are ascribed to the typical stretching modes of CN heterocycles,[23,25,28] and the broad bands in the range of 3000–3500 cm^{-1} are assigned to the stretching vibration modes of O–H or N–H.[23,25,28] The peak at 810 cm^{-1} can be assigned to the out-of-plane bending vibration characteristics of the triazine or heptazine rings, and the one at 888 cm^{-1} is related to deformation mode of N–H.[23,25,28] For pure TiO_2, the absorption band at 400–800 cm^{-1} is due to the

Table 2 Molar ratios of TiO_2/C_3N_4 for $TiO_2@P\text{-}g\text{-}C_3N_4$ composites determined by TGA. x and y are the sample weights measured at 720 °C and 450 °C, respectively

Sample	x (TiO_2, wt%)	y (wt%)	$y-x$ (C_3N_4, wt%)	TiO_2/C_3N_4 (wt ratio)	TiO_2/C_3N_4 (molar ratio)
Ti60–CN	21.12	93.43	72.31	0.29	0.34
Ti180–CN	44.67	92.58	47.91	0.93	1.07
Ti300–CN	57.30	93.96	36.66	1.56	1.80

stretching vibration modes of Ti–O–Ti.[11,16] For the three TiO_2@P-g-C_3N_4 composites, their spectra can be considered as the combination of TiO_2 and g-C_3N_4 spectra, confirming the formation of a heterostructure.

Fig. 4 shows the comparison of SEM morphologies between P-g-C_3N_4 and TiO_2@P-g-C_3N_4 composites. Ti60–CN (Fig. 4(b)) shows rougher surface, and the sheet structure can be better resolved. As the cycle number of TiO_2 increases to 180 cycles (Fig. 4(c)), the structure is still porous and becomes smoother, similar to that of P-g-C_3N_4, Fig. 4(a). When the cycle number is further raised to 300, the porous structure becomes less clear, as shown in Fig. 4(d), presumably because the pores are mostly filled up with TiO_2. EDX mapping of the Ti180–CN composite displays the distribution of the constituent elements, as shown in Fig. 5. Four elements (C, N, Ti, O) are uniformly dispersed in the Ti180–CN composite, confirming that TiO_2 thin film was indeed well deposited on the porous g-C_3N_4 by ALD.

The HRTEM images and the selected area electron diffraction (SAED) patterns of P-g-C_3N_4 and Ti180–CN were taken to further evidence the presence of TiO_2 on P-g-C_3N_4, as shown in Fig. S2.† Based on the SAED pattern, well-crystallized TiO_2 thin film is deposited on P-g-C_3N_4. Furthermore, the inset HRTEM image in Fig. S2(b)† evidences a lattice spacing of 0.352 nm, corresponding to the (101) crystal plane of anatase.

In order to determine the real molar ratios of TiO_2/C_3N_4 in TiO_2@P-g-C_3N_4 composites, TGA analysis was performed from 30 °C to 800 °C to measure the weight loss due to decomposition of carbon nitride, as shown in Fig. S3.† For pure P-g-C_3N_4, it can be completely decomposed when the temperature exceeds 720 °C. For TiO_2@P-g-C_3N_4 composites, carbon nitride starts to decompose at around 500 °C, and could be totally removed when the temperature is above 635 °C. Therefore, the real contents of TiO_2 in the samples can be calculated, as listed in Table 2. It is seen that the molar ratio of TiO_2/C_4N_4 is linearly dependent on the cycle number. Fig. 6 shows the effects of cycle number on the thickness of TiO_2 and specific surface area of the composites. The thicknesses of TiO_2 films on silicon wafer were measured and listed in Table 1, and the growth rate was calculated to be approximately 0.79 Å per cycle. The specific surface areas were obtained by the BET method and also listed in Table 1. For the TiO_2@P-g-C_3N_4 composites, the value decreases from 55.2 to 27.3 $m^2 g^{-1}$ when the TiO_2 cycle number increases from 60 to 300 cycles. With the growth rate of 0.79 Å per cycle, the film thickness of TiO_2 from 300 cycles of ALD can reach 23.7 nm (the actual thickness was 24.69 nm). This implies that the pores in the size of ~50 nm would be almost filled up with TiO_2, resulting in reduced specific surface area.

The N_2 adsorption–desorption isotherms and the corresponding pore size distribution curves of the samples are shown in Fig. 7. P-g-C_3N_4 exhibits type IV curves based on the six isotherm types classified by the International Union of Pure and Applied Chemistry (IUPAC).[33] It indicates the presence of mesopores.[34] Furthermore, it also exhibits H3 adsorption hysteresis loop which may be referred to the existence of slit-like pores in the porous structure of P-g-C_3N_4.[33] This is exactly what was observed in Fig. 1(d). Meanwhile, based on the pore-size distribution both meso and macropores are present in P-g-C_3N_4,[34] especially a large fraction of pores are in the size of 40–80 nm. Fig. 7(b)–(d) show that the isothermal curve types of TiO_2@P-g-C_3N_4 composites are all similar to that of P-g-C_3N_4. However, the volume of pores in the diameter of 20 to 100 nm decreases as the TiO_2 cycle number increases.

To investigate the interaction between TiO_2 and P-g-C_3N_4, XPS analysis was performed. For pure P-g-C_3N_4, the bonding energies of C 1s (Fig. 8(a)) at 288.2 and 284.8 eV correspond to N–C=N and C–C, respectively, and the bonding energies of N 1s (Fig. 8(b)) at 398.7 eV, 399.9 eV, and 401.2 eV correspond to C–N=C, N–(C)$_3$, and C–N–H, respectively.[26,28,29,35] The peak of N–C=N in TiO_2@P-g-C_3N_4 composites has slightly shifted to higher energies than the peak in pure P-g-C_3N_4, which might be ascribed to the bonding between TiO_2 and g-C_3N_4.[36] For pure TiO_2, the binding energy of Ti $2p_{3/2}$ is 458.8 eV. The Ti 2p spectra (Fig. 8(c)) show that the intensity and energy of Ti $2p_{3/2}$ increase with the cycle number of TiO_2, which might be ascribed to the weaker interaction with g-C_3N_4 as the film becomes thicker. To further understand the characteristic of TiO_2 on P-g-C_3N_4, the atomic ratios of Ti/C on the sample surface analyzed by XPS and in the bulk calculated from the molar ratios of TiO_2/C_3N_4 by TGA are compared in Fig. 8(d). Both surface and bulk ratios of Ti/C increase linearly with the TiO_2 cycle number. Furthermore, the surface ratio is three times higher than the bulk ratio. All these results evidence that TiO_2 is present uniformly on P-g-C_3N_4 in the form of thin film.
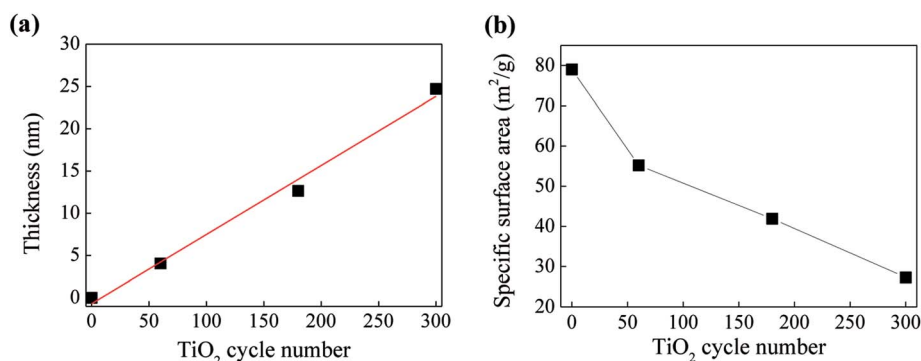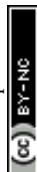

Fig. 6 Dependence of (a) thickness of TiO_2 and (b) specific surface area of the composites on TiO_2 cycle number.
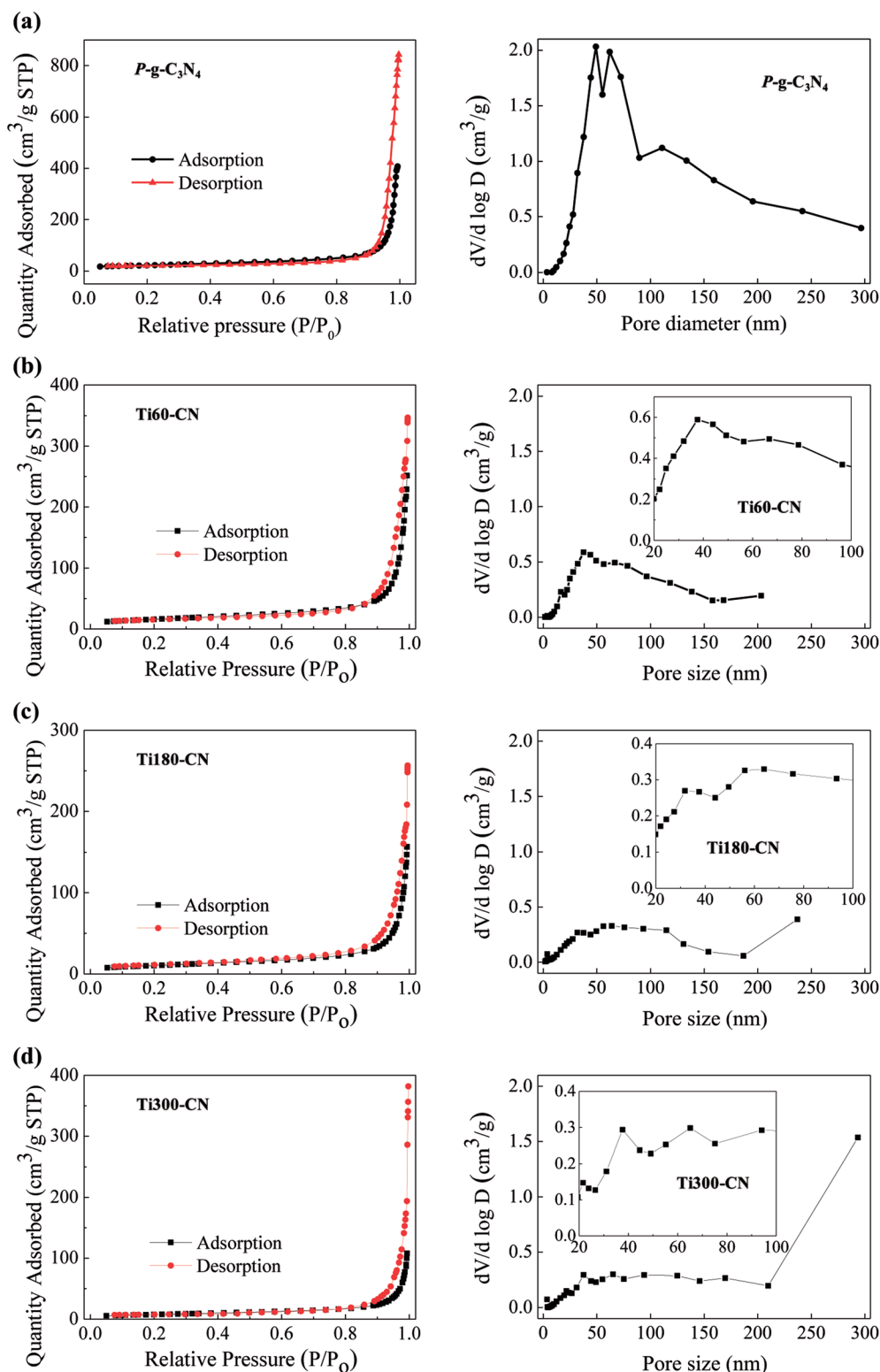
Fig. 7 Adsorption–desorption isotherms (left) and pore-size distributions (right) of (a) P-g-C$_3$N$_4$, (b) Ti60−CN, (c) Ti180−CN, and (d) Ti300−CN. The insets show the magnified pore size distributions in the range of 20–100 nm.

The absorption edges of TiO$_2$@P-g-C$_3$N$_4$ composites remain about the same as that of P-g-C$_3$N$_4$, although a slight blue shift with increasing the TiO$_2$ cycle number can be barely resolved, as shown in Fig. S4.† In order to better understand the photo-catalytic mechanism, the PL analysis has been commonly used to study the recombination behavior of photo-excited electron–
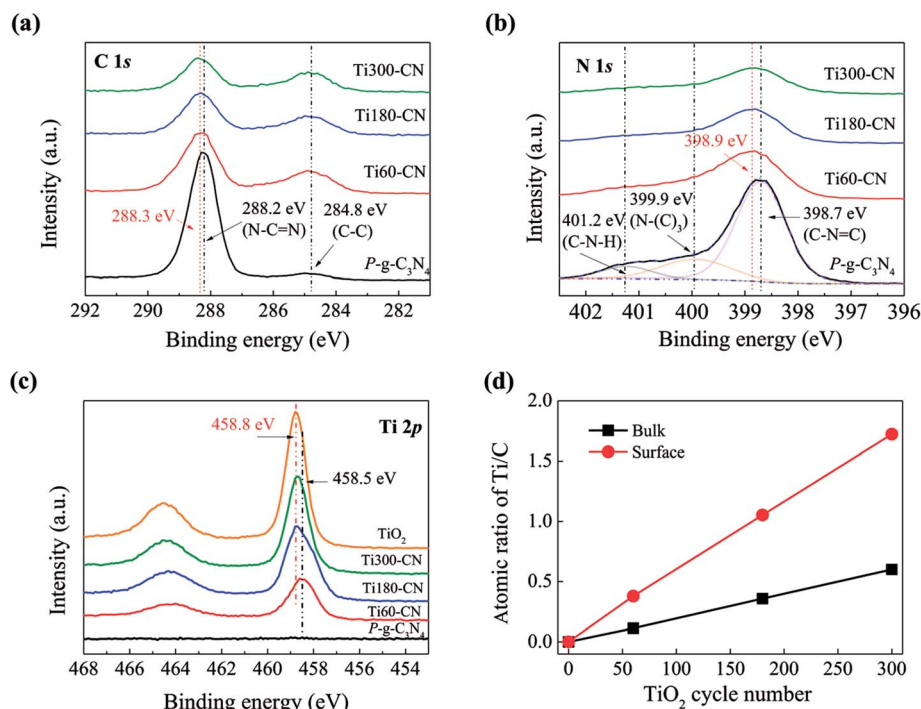
Fig. 8 High-resolution XPS spectra of (a) C 1s, (b) N 1s, and (c) Ti 2p. (d) The bulk and surface ratio of Ti/C with the dependence of TiO_2 cycle number.

hole pairs. Fig. 9 displays that P-g-C_3N_4 exhibits a broad and strong PL emission peak in the range of 400 to 600 nm, corresponding to the recombination of charge carriers of carbon nitride. Compared to P-g-C_3N_4, Ti60–CN shows a lower emission peak in the same range of wavelength, which indicates a lower recombination rate of charge carriers. Ti180–CN shows the lowest emission peak among the TiO_2@P-g-C_3N_4 samples, which is ascribed to the suitable thickness that provides more efficient transport of electrons. Therefore, the TiO_2@P-g-C_3N_4 heterostructure would enhance the photocatalytic activity due to the lower recombination rate, and the activity is related to the thickness of the TiO_2 film.

C. Hydrogen generation from the TiO_2@P-g-C_3N_4 composites

The hydrogen generation rates from the methanol aqueous solution by the TiO_2@P-g-C_3N_4 composites loaded with 30 cycles of Pt were evaluated under 300 W Xe lamp illumination with a solar filter, as shown in Fig. 10. With 30 cycles of Pt on
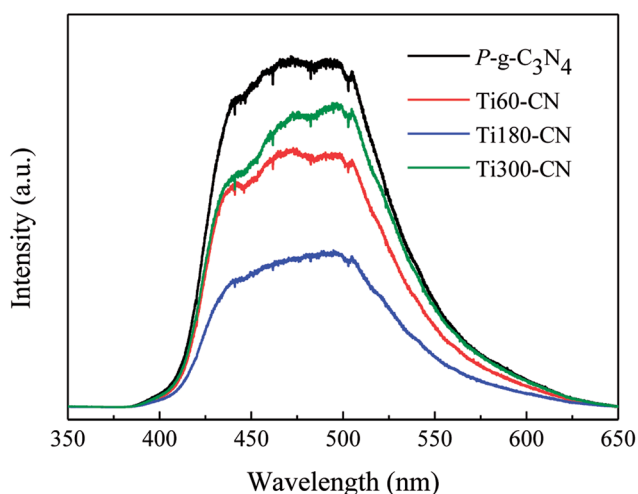

Fig. 9 PL spectra of pure P-g-C_3N_4 and TiO_2@P-g-C_3N_4 composites. All samples were deposited with Pt by 30 ALD cycles.
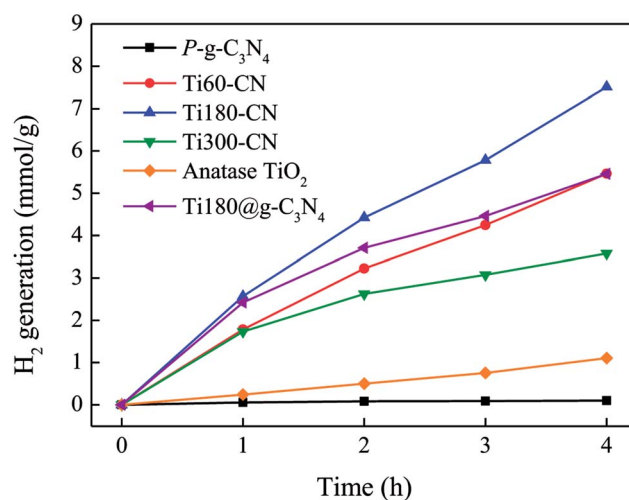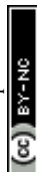

Fig. 10 H_2 evolution generation rate from 20 vol% methanol aqueous solution under 300 W Xe lamp with a solar filter. All samples were deposited with Pt by 30 ALD cycles.
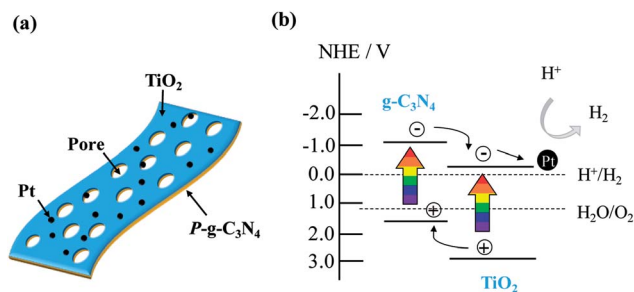
Fig. 11 (a) Schematic of Pt-loaded TiO$_2$@P-g-C$_3$N$_4$ 2D/2D heterojunction structure. (b) Proposed mechanism of charge transfer for photocatalytic H$_2$ evolution from Pt-loaded TiO$_2$@P-g-C$_3$N$_4$.

TiO$_2$@P-g-C$_3$N$_4$, the Pt loading is ~0.3 wt%, similar to our previous result.[22] Commercial anatase TiO$_2$ (Riedel-de Haën, 99%) and pure P-g-C$_3$N$_4$, both were also loaded with Pt, were used as the control specimens. All of the TiO$_2$@P-g-C$_3$N$_4$ composites show higher H$_2$ production rates than anatase (0.26 mmol g^{-1} h^{-1}) and P-g-C$_3$N$_4$ (0.03 mmol g^{-1} h^{-1}). Among the TiO$_2$@P-g-C$_3$N$_4$ composites, Ti180–CN shows the highest H$_2$ production rate (1.96 mmol g^{-1} h^{-1}) because of the suitable thickness (~13 nm), consistent with prediction from the PL analysis.[37,38] When an additional specimen prepared with 180 cycles of TiO$_2$ deposited on g-C$_3$N$_4$ (Ti180@g-C$_3$N$_4$) was also tested for comparison, it is seen that Ti180–CN exhibited 31% higher H$_2$ generation rate than Ti180@g-C$_3$N$_4$ (1.50 mmol g^{-1} h^{-1}). It confirms that the porous structure of P-g-C$_3$N$_4$ indeed has enhanced photocatalytic activity.

To further confirm the behavior of photogenerated charge carriers, the photoelectrochemical properties of P-g-C$_3$N$_4$, TiO$_2$ (180 cycles), and Ti180–CN samples were evaluated using a three-electrode cell under 150 W Xe lamp illumination with a solar filter. The result is shown in Fig. S5.† It is seen that the heterojunction structure has indeed improved the efficiency of charge carrier separation, resulting in a higher photocurrent density.

A schematic of Pt-loaded TiO$_2$@P-g-C$_3$N$_4$ 2D/2D (2-dimensional) structure and the mechanism for photocatalytic H$_2$ evolution by the composite are illustrated in Fig. 11. Porous g-C$_3$N$_4$ thin sheet is a 2D photocatalyst, which is an ideal form to produce H$_2$ due to fast transport rate and low recombination rate of charge carriers.[7] Using ALD to deposit TiO$_2$ uniformly on P-g-C$_3$N$_4$ would further improve photocatalytic activity due to fast transport rate caused by the large contact interface.[39] The electrons would easily migrate to the surface and accumulate on the Pt nanoparticles to reduce H$^+$ to H$_2$. Therefore, TiO$_2$@P-g-C$_3$N$_4$ 2D/2D photocatalysts loaded with Pt nanoparticles as cocatalyst show improved H$_2$ production under solar illumination.

4. Conclusion

P-g-C$_3$N$_4$ thin sheet was fabricated by calcining the mixture of urea, melamine, and ammonia chloride. Compared to conventional urea-derived g-C$_3$N$_4$ nanosheet, P-g-C$_3$N$_4$ shows higher H$_2$ production efficiency, mainly attributed to enhanced optical absorption in visible light and lower recombination rate of charge carriers because of the porous structure. P-g-C$_3$N$_4$ was used as a template to deposit TiO$_2$ with various thicknesses by ALD to fabricate 2D/2D heterostructure photocatalysts. The thickness of TiO$_2$ could be precisely controlled by the cycle number with a growth rate of 0.79 Å per cycle. Because TiO$_2$ was deposited uniformly on P-g-C$_3$N$_4$ in the form of thin film, the specific surface area of the composite was decreased, and the surface atomic ratio of Ti/C was three times higher than the bulk ratio. Compared to pure P-g-C$_3$N$_4$ and anatase TiO$_2$, all the TiO$_2$@P-g-C$_3$N$_4$ composites showed much higher hydrogen evolution rates. Among them, Ti180–CN exhibited the best performance. It also outperformed Ti180@g-C$_3$N$_4$. Therefore, P-g-C$_3$N$_4$ coupled with TiO$_2$ to form a 2D/2D heterostructure offers promising application in photocatalysis of water to produce hydrogen.

Conflicts of interest

There are no conflicts to declare.

Acknowledgements

References

1 X. C. Wang, K. Maeda, A. Thomas, K. Takanabe, G. Xin, J. M. Carlsson, K. Domen and M. Antonietti, *Nat. Mater.*, 2009, **8**, 76–80.

2 T. Jafari, E. Moharreri, A. S. Amin, R. Miao, W. Q. Song and S. L. Suib, *Molecules*, 2016, **21**, 900.

3 M. R. Hoffmann, S. T. Martin, W. Y. Choi and D. W. Bahnemann, *Chem. Rev.*, 1995, **95**, 69–96.

4 K. Maeda, M. Higashi, D. L. Lu, R. Abe and K. Domen, *J. Am. Chem. Soc.*, 2010, **132**, 5858–5868.

5 K. Maeda, *J. Photochem. Photobiol., C*, 2011, **12**, 237–268.

6 X. Li, J. G. Yu, J. X. Low, Y. P. Fang, J. Xiao and X. B. Chen, *J. Mater. Chem. A*, 2015, **3**, 2485–2534.

7 T. M. Su, Q. Shao, Z. Z. Qin, Z. H. Guo and Z. L. Wu, *ACS Catal.*, 2018, **8**, 2253–2276.

8 D. J. Martin, P. J. T. Reardon, S. J. A. Moniz and J. W. Tang, *J. Am. Chem. Soc.*, 2014, **136**, 12568–12571.

9 G. X. Zhao, X. B. Huang, F. Fina, G. Zhang and J. T. S. Irvine, *Catal. Sci. Technol.*, 2015, **5**, 3416–3422.

10 J. Q. Yan, H. Wu, H. Chen, Y. X. Zhang, F. X. Zhang and S. F. Liu, *Appl. Catal., B*, 2016, **191**, 130–137.

11 H. Zhang, F. Liu, H. Wu, X. Cao, J. H. Sun and W. W. Lei, *RSC Adv.*, 2017, **7**, 40327–40333.

12 Q. Zhang, H. Wang, S. Chen, Y. Su and X. Quan, *RSC Adv.*, 2017, **7**, 13223–13227.

13 A. P. Singh, P. Arora, S. Basu and B. R. Mehta, *Int. J. Hydrogen Energy*, 2016, **41**, 5617–5628.

14 W. J. Ong, L. L. Tan, Y. H. Ng, S. T. Yong and S. P. Chai, *Chem. Rev.*, 2016, **116**, 7159–7329.

15 C. Pan, J. Jia, X. Y. Hu, J. Fan and E. Z. Liu, *Appl. Surf. Sci.*, 2018, **430**, 283–292.

16 C. L. Wang, L. M. Hu, B. Chai, J. T. Yan and J. F. Li, *Appl. Surf. Sci.*, 2018, **430**, 243–252.

17 L. N. Ma, G. H. Wang, C. J. Jiang, H. L. Bao and Q. C. Xu, *Appl. Surf. Sci.*, 2018, **430**, 263–272.

18 S. H. Huang, C. C. Wang, S. Y. Liao, J. Y. Gan and T. P. Perng, *Thin Solid Films*, 2016, **616**, 151–159.

19 K. I. Liu, C. C. Kei, M. Mishra, P. H. Chen, W. S. Liu and T. P. Perng, *RSC Adv.*, 2017, **7**, 34730–34735.

20 K. I. Liu, C. Y. Su and T. P. Perng, *RSC Adv.*, 2015, **5**, 88367–88374.

21 H. S. Chen, P. H. Chen, J. L. Kuo, Y. C. Hsueh and T. P. Perng, *RSC Adv.*, 2014, **4**, 40482–40486.

22 C. C. Wang, Y. C. Hsueh, C. Y. Su, C. C. Kei and T. P. Perng, *Nanotechnology*, 2015, **26**, 254002.

23 W. Iqbal, C. Y. Dong, M. Y. Xing, X. J. Tan and J. L. Zhang, *Catal. Sci. Technol.*, 2017, **7**, 1726–1734.

24 S. C. Yan, Z. S. Li and Z. G. Zou, *Langmuir*, 2009, **25**, 10397–10401.

25 J. Y. Xu, Y. X. Li, S. Q. Peng, G. X. Lu and S. B. Li, *Phys. Chem. Chem. Phys.*, 2013, **15**, 7657–7665.

26 S. W. Cao, J. X. Low, J. G. Yu and M. Jaroniec, *Adv. Mater.*, 2015, **27**, 2150–2176.

27 P. X. Qiu, H. Chen, C. M. Xu, N. Zhou, F. Jiang, X. Wang and Y. S. Fu, *J. Mater. Chem. A*, 2015, **3**, 24237–24244.

28 D. Q. Feng, Y. H. Cheng, J. He, L. C. Zheng, D. W. Shao, W. C. Wang, W. H. Wang, F. Lu, H. Dong, H. Liu, R. K. Zheng and H. Liu, *Carbon*, 2017, **125**, 454–463.

29 P. Niu, L. L. Zhang, G. Liu and H. M. Cheng, *Adv. Funct. Mater.*, 2012, **22**, 4763–4770.

30 W. J. Jiang, W. J. Luo, J. Wang, M. Zhang and Y. F. Zhu, *J. Photochem. Photobiol., C*, 2016, **28**, 87–115.

31 Y. W. Zhang, J. H. Liu, G. Wu and W. Chen, *Nanoscale*, 2012, **4**, 5300–5303.

32 S. Rajaambal, K. Sivaranjani and C. S. Gopinath, *J. Chem. Sci.*, 2015, **127**, 33–47.

33 M. Thommes, K. Kaneko, A. V. Neimark, J. P. Olivier, F. Rodriguez-Reinoso, J. Rouquerol and K. S. W. Sing, *Pure Appl. Chem.*, 2015, **87**, 1051–1069.

34 Z. A. ALOthman, *Materials*, 2012, **5**, 2874–2902.

35 Q. Su, J. Sun, J. Q. Wang, Z. F. Yang, W. G. Cheng and S. J. Zhang, *Catal. Sci. Technol.*, 2014, **4**, 1556–1562.

36 T. Giannakopoulou, I. Papailias, N. Todorova, N. Boukos, Y. Liu, J. G. Yu and C. Trapalis, *Chem. Eng. J.*, 2017, **310**, 571–580.

37 A. K. Chandiran, P. Comte, R. Humphry-Baker, F. Kessler, C. Y. Yi, M. K. Nazeeruddin and M. Gratzel, *Adv. Funct. Mater.*, 2013, **23**, 2775–2781.

38 S. H. Huang, S. Y. Liao, C. C. Wang, C. C. Kei, J. Y. Gan and T. P. Perng, *Nanotechnology*, 2016, **27**, 405702.

39 B. Lin, H. Li, H. An, W. B. Hao, J. J. Wei, Y. Z. Dai, C. S. Ma and G. D. Yang, *Appl. Catal., B*, 2018, **220**, 542–552.